




Article

Control and Suppression of Vortex Shedding from a Slightly Rough Circular Cylinder by a Discrete Vortex Method

Marcos André de Oliveira ¹, Paulo Guimarães de Moraes ¹, Crystianne Lilian de Andrade ¹, Alex Mendonça Bimbato ² and Luiz Antonio Alcântara Pereira ^{1,*}

¹ Mechanical Engineering Institute, Federal University of Itajubá (UNIFEI), Itajubá MG 37.500-903, Brazil; marcos.oliveira@uft.edu.br (M.A.d.O.); pauloguimor@gmail.com (P.G.d.M.); cristiannelilian@yahoo.com.br (C.L.d.A.)

² School of Engineering, São Paulo State University (UNESP), Guaratinguetá SP 12.516-410, Brazil; alex.bimbato@unesp.br

* Correspondence: luizantp@unifei.edu.br; Tel.: +55-21-35-3629-1041

Received: 31 July 2020; Accepted: 26 August 2020; Published: 31 August 2020



Abstract: A discrete vortex method is implemented with a hybrid control technique of vortex shedding to solve the problem of the two-dimensional flow past a slightly rough circular cylinder in the vicinity of a moving wall. In the present approach, the passive control technique is inspired on the fundamental principle of surface roughness, promoting modifications on the cylinder geometry to affect the vortex shedding formation. A relative roughness size of $\varepsilon^*/d^* = 0.001$ (ε^* is the average roughness and d^* is the outer cylinder diameter) is chosen for the test cases. On the other hand, the active control technique uses a wall plane, which runs at the same speed as the free stream velocity to contribute with external energy affecting the fluid flow. The gap-to-diameter varies in the range from $h^*/d^* = 0.05$ to 0.80 (h^* is the gap between the moving wall and the cylinder bottom). A detailed account of the time history of pressure distributions, simultaneously investigated with the time evolution of forces, Strouhal number behavior, and boundary layer separation are reported at upper-subcritical Reynolds number flows of $Re = 1.0 \times 10^5$. The saturation state of the numerical simulations is demonstrated through the analysis of the Strouhal number behavior obtained from temporal history of the aerodynamic loads. The present work provides an improvement in the prediction of Strouhal number than other studies no using roughness model. The aerodynamic characteristics of the cylinder, as well as the control of intermittence and complete interruption of von Kármán-type vortex shedding have been better clarified.

Keywords: bluff body; roughness model; Venturi effect; suppression hybrid control; Lagrangian description

1. Introduction

In the literature, “bluff body” is defined as being a structure that when immerse in a fluid flow will present significant proportion of its surface generating separated flow. This idea is also associated with characteristics of the flow around the body, especially the two shear layers of opposite signals formed from the separation points of the body [1]. Since 1900, numerous analytical, numerical, and experimental investigations have been conducted to study bluff body aerodynamics on either two-dimensional or axisymmetric shapes; the two most common bodies being the circular cylinder and the sphere. The more relevant results have contributed to develop important researches in aerospace/aeronautical, civil, marine, mechanical, and computer engineering.

The present paper aims to contribute with more discussions concerning the surface roughness effect on bluff body aerodynamics. An important practical engineering application of the flow around cylindrical structures is that of the fluid–elastic interaction between the flow and the structure exciting the body into flow-induced vibrations (FIV) [2–6]. Undoubtedly, the surface roughness effect must be used to control this non-linear hydrodynamic phenomenon. This is one of important motivations for future extension of our present research, which will also include the study of slender body aerodynamics [7]. Another one is planned to investigate heat transfer behavior in mixed convection of a fluid by a temperature particles method [8].

In the context of the present work, the literature has reported studies of surface roughness effect on flow past a bluff body with low frequency [2,5,6,9–19]. It is important to mention that numerical analysis of rough bluff body aerodynamics near a ground plane is very limited, which valorizes the recent methodology proposed by Alcântara Pereira et al. [10] and classified such as “hybrid control technique of vortex shedding” [20].

In fact, control and suppression of vortex shedding from a bluff body has been considered as one of the most important research areas in the field of aerodynamics and hydrodynamics applications, such as vibration of pipelines, interactions of currents and wave with offshore structures, suspension bridges and chimneys near tall buildings.

There are different situations where the vortex shedding may cease, and, of particular interest here, is that of a circular cylinder in the vicinity of a ground plane. To the best of our knowledge, the ground effect is governed by three mechanisms [21–28]: (i) The wake interference because of the intertwine of the body wake and the boundary layer formed on the ground, the latter is less influent despite several intensive studies reported so far. (ii) The three-dimensional effect, which presents a momentum transfer in the axial direction of the body leading to a lower drag force value as compared to the two-dimensional results. (iii) The blockage effect (or Venturi effect), which contributes to appearing big and small peaks during the temporal evolution of the drag curve. These peaks have been identified within the large-gap regime, i.e., $h^*/d^* > 0.40$, by Bimbato et al. [22] using a discrete vortex method implemented with Large Eddy Simulation (LES) theory. The large-gap regime is characterized by the presence of strong vortical structures, which are generated at the rear part of a bluff body [25]. In Section 3.2, these peculiar peaks' behavior on the drag curve will be again studied, now using the present numerical method, to contribute on discussion of the roughness model sensitivity. The applicability of the Venturi effect in aerodynamic models has been discussed in the literature [29,30].

Within the scenario above described, Roshko et al. [26] reported the aerodynamic forces behavior for the smooth circular cylinder in the vicinity of a fixed wall using a wind tunnel at high Reynolds number flow of $Re = 2.0 \times 10^4$. As the cylinder came close to the ground plane, it was reported that the drag force rapidly decreased; on the contrary, the lift force increased.

Zdravkovich [27] also reported aerodynamic forces behavior for the smooth circular cylinder near a fixed ground at high Reynolds numbers flows in the range of $4.8 \times 10^4 < Re < 3.0 \times 10^5$. As the gap-to-diameter ratio h^*/d^* , reduced to less than the thickness of the boundary layer δ^*/d^* (δ^* is the boundary layer thickness) on the ground plane, it was identified a rapid decrease in the drag force. The drag variation was dominated by h^*/δ^* and the ratio h^*/d^* was less dominant. It was observed that the state of the boundary layer could interfere in the lift force, although the boundary layer thickness was less influent.

In other relevant research, Zdravkovich [28] investigated the drag force behavior of the smooth circular cylinder near a ground plane. The wall plane ran at the same speed as the free stream velocity in an upper-subcritical Reynolds number flow of $Re = 2.5 \times 10^5$ into the critical flow regime. The experimental results showed contrast to all previous studies using fixed ground, e.g., [26,27], because practically no boundary layer was generated from the moving wall. Interestingly, the expected decrease of the drag force, as the ratio h^*/d^* decreased, did not appear. That behavior was attributed to the non-existence of the boundary layer formed on the ground or the high Reynolds number, or any other influencing factors, such as surface texture and structural vibration.

Nishino [25] reported experimental results of the flow around the smooth circular cylinder with an aspect ratio of 8.33 in a wind tunnel. Two upper-subcritical Reynolds numbers of $Re = 0.4 \times 10^4$ and 1.0×10^5 were investigated during his experiments. The cylinder with and without end plates configurations were near and parallel to a wall plane running at the same speed as the free stream velocity. The moving wall effect eliminated the less influential effects of boundary layer formed on the ground and, therefore, the experimental results contributed to clarify the fundamental mechanisms of ground effect in more details. The experimental study also produced new perceptions into the physics of ground effect, and still nowadays serves as database to support numerical investigations. Of importance for the present work, is that, for the cylinder with end plates, the oil flow patterns were observed to be approximately two-dimensional. In contrast to the cylinder near a fixed ground configuration [26], the drag force rapidly decreased, as the ratio h^*/d^* decreased to less than 0.50 and became constant for h^*/d^* of less than 0.35.

Bimbato et al. [21,22] implemented an algorithm of the discrete vortex method with LES modeling to study the two-dimensional flow around the circular cylinder near a moving wall. Their numerical strategy was to represent the ground plane motion using a plane wall with no vorticity generation on it. The numerical results for an upper-subcritical Reynolds number of $Re = 1.0 \times 10^5$ presented a good agreement with the experimental results reported by Nishino [25] using the cylinder with end plates configuration. The authors concluded that the Venturi effect almost completely suppressed the vortex shedding from the cylinder placed closer to the ground plane. Furthermore, the drag force decreased as consequence of the suppression.

In a recent paper, Alcântara Pereira et al. [10] proposed a hybrid control technique of vortex shedding, combining passive and active controls, to study the flow past the rough circular cylinder in the vicinity of a moving wall at upper-subcritical Reynolds number of $Re = 1.0 \times 10^5$. They successfully associated the methodologies developed by Bimbato et al. [11,21,22] focusing on the effect of higher relative roughness sizes, namely, $\varepsilon^*/d^* = 0.0045$ and 0.007 , on flow dynamics of the cylinder at small-gap regime, which was identified in past investigation by Bimbato et al. [22] at $h^*/d^* < 0.20$. The small-gap regime is characterized by vortex shedding suppression. Their results shown an anticipation of the vortex shedding suppression when using $\varepsilon^*/d^* = 0.007$ at $h^*/d^* = 0.10$. Of importance, the Strouhal number completely vanished ($St = 0.0$) and it was observed the formation of two nearly parallel shear layers of opposite signals at the rear part of the cylinder. It is interesting to comment that Bimbato et al. [22] did not capture the complete interruption of vortex shedding, even at $h^*/d^* = 0.05$. This flow behavior will be investigated later in Section 3.2 to also contribute on discussion of the roughness model effect on it.

It is important to observe that Alcântara Pereira et al. [10] only computed the form component of the drag force. According to the discussions of Achenbach [9], the form (or pressure) component dominates the drag force on the smooth cylinder contributing more than 98% of the total drag force. On the other hand, the skin friction (or viscous) component of the drag force is responsible for the remaining 1–2%. In the literature, it is expected neither component of the drag force of the rough cylinder can be neglected. However, Achenbach [9] investigated the viscous drag force from a sand-roughened surface ($\varepsilon^*/d^* = 0.0011$ and 0.0045) and concluded that it contributed about 2–3% of the total drag force. That result showed a slight increase of the viscous drag force as compared as that of the smooth cylinder. Alcântara Pereira et al. [10] have reported differences above 10% between the smooth cylinder and other rough when integrating only static pressure, and, therefore, as discussed by them, the surface roughness effect has been captured by their numerical approach.

The main contribution of the present paper is shown that the methodology proposed by Alcântara Pereira et al. [10] also captures important changes in the flow dynamics of the slightly rough circular cylinder in the vicinity of a moving wall. Thus, the effect of small relative roughness size, namely, $\varepsilon^*/d^* = 0.001$, on flow dynamics around the cylinder is investigated and compared to smooth cylinder configurations. The chosen roughness size can be found, for example, in support columns of large offshore floating structures after a few years of operation. Put in other words, the main goal here is to

report understanding of the influence of surface roughness for control of vortex shedding frequency reduction and wake destructive behavior behind the rough cylinder placed near a moving wall at upper-subcritical Reynolds number of $Re = 1.0 \times 10^5$. Our highlight results are for temporal history of aerodynamic loads, Strouhal number behavior and separation point prediction. The focus is to track the Strouhal number behavior until it vanishes. Overall, the results are found agree with the physics expected for this kind of vortical flow. The Section 4 will summarize the key findings of this study.

The rough circular cylinder aerodynamics has been reasonably reported in the literature [2,9,11,12,14,16,18], however, very little attention has been paid to the problem of the flow around the rough cylinder near a moving wall [10]. In recent past works [10,11], it has been reported that the effect of two-dimensional roughness model is much more sensitive than single turbulence modeling.

In general, numerical simulations of high Reynolds number flows around two-dimensional bluff bodies over predict aerodynamic forces behavior. However, the results are very important for applications of conservative designs in practical engineering problems, where higher integrated loads are computed, specially the drag force, in association with accurate vortex shedding frequencies. In the last years, our research group has made an effort to develop the in-house code for future extension to three-dimensional flows, and this research is integral part of the project.

2. Theory and Numerical Method

2.1. Physical Modeling

Figure 1 illustrates the smooth circular cylinder immersed in a semi-infinity fluid domain, Ω , with a free stream velocity, U^* , at infinity. The fluid is Newtonian with constant kinematic viscosity, ν . The flow is assumed to be unsteady, incompressible, and two-dimensional. The fluid domain can be identified by a surface $S = S_1 \cup S_2 \cup S_3$, being S_1 the cylinder surface, S_2 the moving wall surface and S_3 the far away boundary. The surface S is required to establish the boundary conditions of the physical problem. The location of the separation points of the flow for the top (open) and the bottom (gap) sides of the cylinder are defined by θ^+_{sep} and θ^-_{sep} , respectively. The blockage effect is captured by reducing the gap-to-diameter ratio, h^*/d^* .

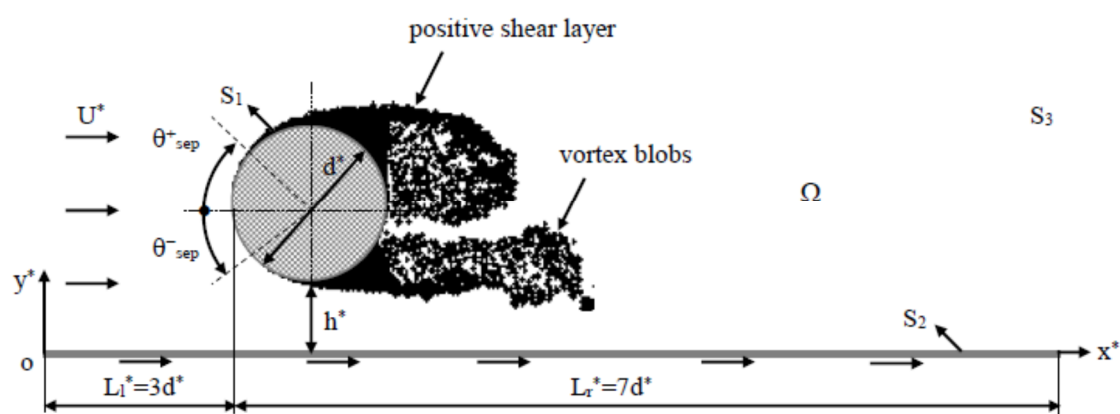


Figure 1. Schematic representation of the semi-infinity fluid domain.

To non-dimensionalize all the quantities of the problem, it is chosen the cylinder diameter, d^* , as scale length. The dimensionless time is defined by t^*U^*/d^* . In the general formulation, the symbol $*$ is used to identify dimensional quantities.

The Reynolds number is defined in the following form:

$$Re = \frac{U^* d^*}{\nu} \quad (1)$$

According to Bearman [1], the presence of two shear layers of opposite signals is primarily responsible for vortex shedding, and the body merely modifies the mechanism by allowing feedback between the viscous wake and the shedding of circulation at the separation points (Figure 1). As consequence, the interaction between the two shear layers as a function of the free stream velocity, U^* , and the body diameter, d^* , is the key factor to define the rate at which vortical structures are cyclically detached at the rear part of the body. Thus, the dimensionless Strouhal number is defined as:

$$St = f^* \frac{d^*}{U^*} \quad (2)$$

being the frequency of vortex shedding, f^* , related with the scales d^* and U^* .

The Strouhal number for the smooth cylinder with no wall confinement has been experimentally measured in the literature and found close to $St \approx 0.19$ for an upper-subcritical Reynolds number of $Re = 1.0 \times 10^5$ [31]. In Equation (2), the quantity f^* is originally obtained from the temporal series of the lift force curve.

2.2. Introduction of Source Singularity Elements and Nascent Vortex Blobs

In the present numerical method, the smoothed cylinder and moving wall surfaces (Figure 1) are treated by an integral formulation of the potential component of the flow [32]. These surfaces are discretized and represented by flat panels with distribution of source singularity elements with constant density. Each flat panel has a center point, named pivotal point, where the impermeability boundary condition must be satisfied. The impermeability condition is imposed on each pivotal point and it establishes equality between the normal velocity component of a fluid particle and the normal velocity component of each pivotal point. Of numerical importance is the fact that the impermeability condition and the mass conservation of the problem are guaranteed by the source elements generation in each temporal step.

In addition to this, the discrete vortex method engages in to discretize spatially the vorticity field using an instantaneous vortex blobs collection, as illustrated in Figure 1. The vortex blobs are represented by Lamb vortex elements, each one presenting a distribution of vorticity, ζ_{σ_0} , (commonly called the cut-off function), a circulation strength, Γ , a core size, σ_0 , and a spatial position, x [33,34]. The no-slip boundary condition is imposed on each pivotal point and it establishes equality between the tangential velocity component of a fluid particle and the tangential velocity component of each pivotal point. Of numerical importance is the fact that the no-slip condition and the global circulation conservation of the problem are guaranteed by the vortex blobs generation in each temporal step. The moving wall effect dispenses this boundary condition on the ground plane, being the vortex blobs only generated on the cylinder surface [21,22,25]. Figure 2 illustrates as a vortex blob is introduced into the fluid domain. In Lagrangian manner, the vorticity generated from a flat panel stay concentrated inside blob vortex core, σ_0 .

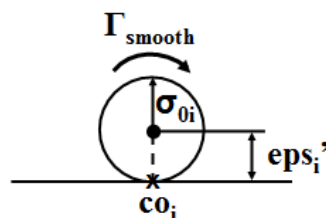


Figure 2. Shedding of a vortex blob during one time stepping (co_i is the pivotal point and ϵ_{ps_i}' defines the “smooth shedding point” location of the vortex blob).

To satisfy the boundary conditions above mentioned are necessary two different kinds of system of linear algebraic equations, which are solved iteratively using the method of least squares. The simultaneous generation of sources elements and vortex blobs can also be coupled with the

roughness model, when activated; details of the roughness model used in simulations of interest will be presented in Section 2.4.

2.3. Discrete Vortex Method with LES Modeling

The motion of each vortex blob is governed by the vorticity transport equation, which is obtained by taking the curl of the Navier–Stokes equations [33]. Chorin [35] proposed an algorithm that splits the vorticity transport equation to separately solve the advection and diffusion problems. Alcântara Pereira et al. [36] originally presented the solution of the two problems including LES modeling into the two-dimensional discrete vortex method, such as, respectively:

$$\frac{D\bar{\omega}}{Dt} = \frac{\partial\bar{\omega}}{\partial t} + (\bar{\mathbf{u}} \cdot \nabla)\bar{\omega} = 0 \quad (3)$$

$$\frac{\partial\bar{\omega}}{\partial t} = \left(\frac{1}{Re} + \nu_t^*\right)\nabla^2\bar{\omega} \quad (4)$$

where

$$\nu_t^* = \frac{\nu_t}{U^*d^*} \quad (5)$$

represents the local eddy viscosity coefficient and $\bar{\omega} = \nabla \times \bar{\mathbf{u}}$ defines the vorticity scalar field.

The vorticity generated from each flat panel in a time stepping is regarded “free” to undergo advection and diffusion process satisfying Equations (3) and (4), respectively. The vortex blobs transport by advection (Equation (3)) is computed through the following expression:

$$\mathbf{x}_i^{t+\Delta t} = \mathbf{x}_i^t + u(\mathbf{x}_i)^{t+\alpha\Delta t} \Delta t = \mathbf{x}_i^t + \left[(K * \bar{\omega})(\mathbf{x}) + \overline{ub}_i^n(\mathbf{x}_i) + 1 \right]^{t+\alpha\Delta t} \Delta t \quad (6)$$

where $u(\mathbf{x}_i)^{t+\alpha\Delta t}$ represents the velocity vector of the filtered field, and α is the temporal integrating parameter, such that $0 \leq \alpha \leq 1$, where $\alpha = 0$ and $\alpha = 1$ define an explicit and an implicit Euler scheme, respectively. In this work, is adopted an explicit Euler scheme.

In Equation (6), the velocity vector is computed at the point occupied by the i th vortex blob according to the Biot–Savart law (vortex–vortex interaction), panel method (vortex–panel interaction) and free stream velocity (vortex–mainstream interaction) contributions, respectively. It is remarkable that the Lagrangian manner [37] dispenses the need to explicitly treat advective derivatives into the Equation (3).

Equation (4) is solved using to the random walk method [35], where is imposed a displacement for each vortex blob in the following form [36]:

$$\zeta_i(t) = \sqrt{\frac{4\Delta t}{Re_{c_i}} \ln\left(\frac{1}{p}\right)} \left[\cos(2\pi Q)_x + \sin(2\pi Q)_y \right] \quad (7)$$

being p and Q random numbers generated between 0.0 and 1.0, and Re_c the local Reynolds number modified by the local eddy viscosity coefficient, such as [36]:

$$Re_{c_i}(t) = \frac{U^*d^*}{\nu + \nu_{t_i}(t)} \quad (8)$$

In Equation (7), p and Q define two random displacements with mean equal to zero and a variance given by twice the product of the kinematic viscosity and the time. The vorticity diffusion process through the random displacements of vortex blobs simulates the viscosity effect.

In the present formulation, the local turbulence effect is simulated during the vorticity diffusion process. Therefore, the local eddy viscosity coefficient computation is necessary to include the effect of the small scales through the concept of differences of velocity between vortex blobs [36]. The support to the turbulence modeling success is that each vortex blob needs to move with the local fluid velocity

in a Lagrangian manner to simulate the vorticity advection process, and the velocity induced at each vortex blob (see $u(x_i)^{t+\alpha \Delta t}$ in Equation (6)) is calculated before the vorticity diffusion process.

The average velocity differences are required to calculate the second-order velocity structure function of the filtered field [38] for each vortex blob that constructs the viscous wake. Alcântara Pereira et al. [36] proposed an adaption to compute the second-order velocity structure function in two-dimensions, such as:

$$\bar{F}_{2j} = \frac{1}{N} \sum_{k=1}^N \|\bar{u}_{t_j}(x_j) - \bar{u}_{t_j}(x_j + r_k)\|_k^2 \left(\frac{\sigma_{0j}}{r_k}\right)^{2/3} \quad (9)$$

where j defines the position of j th vortex blob, \bar{u}_t defines the velocity filtered field computed at each vortex blob, N characterizes a special group of vortex blobs inside a circular crown idealized around the j th vortex blob under analysis, and r_k measures the distance between the j th and k th vortex blobs, the latter necessarily belonging to that special group (for more details, please see Bimbatto et al. [11]).

After the solution of Equation (9), the local eddy viscosity coefficient computation is obtained through the following formula [38]:

$$v_{t_i}(t) = 0.105 C_k^{-3/2} \sigma_{0k} \sqrt{\bar{F}_{2i}(t)} \quad (10)$$

being $C_k = 1.4$ the Kolmogorov constant.

It is important comment that use of two-dimensional LES-based turbulence modeling is necessary to stabilize the numerical solution of the problem; furthermore, it also provides a basis for a future three-dimensional turbulence modeling. Bimbatto et al. [21,22] validated the LES modeling used in this work.

As already mentioned in Section 2.2, the smoothed cylinder surface is represented by source flat panels [32], being that each one also produces one vortex blob of strength Γ_i at every time stepping. Over a period of time, the viscous boundary layer develops to take on the form of a cluster of several thousand vortex blobs, as can be seen from the computer output shown in Figure 3. The separation that occurs on the cylinder surface originates an unsteady flow with the presence of Von Kármán large-scale vortices downstream the body. The proximity of a moving wall (blockage effect) will certainly interfere in any way with that vortex formation regime.

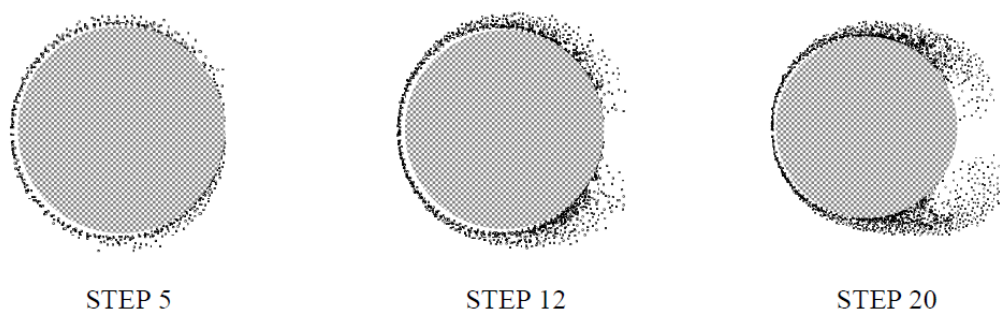


Figure 3. Starting flow around the smooth circular cylinder with no wall confinement.

It is remarkable that with the Lagrangian tracking of vortex blobs, one need not take into account the far away boundary conditions, i.e., at S_3 in Figure 1. In addition, the computations are only concentrated on regions containing significant vorticity, which are the regions of high activities of the flow. The Lagrangian formulation of the discrete vortex method indeed dispenses a grid for the spatial discretization of the interest domain. Thus, numerical instabilities associated to high Reynolds number flows do not require special care in contrast to the Eulerian schemes. In order to take care of both advection and diffusion of the vorticity, one makes use of an advection-diffusion splitting

algorithm [35]; according to it the advection of each vortex blob is carried out independently of the diffusion (Equations (6) and (7)). In other cases, when vortex blobs migrate to the interior of a solid surface, they are reflected from their paths.

2.4. The Roughness Model

The surface roughness effect is associated with the vortex blobs creation process, such that the circulation strength, Γ_{smooth} , of each nascent vortex blob is increased by the amount of $\Delta\Gamma$. The value of $\Delta\Gamma$ is defined by the turbulent activity around a “smooth shedding point” (Figure 2) and accounting by changing the vorticity of the nascent vortex blob. Adjacent to each flat panel, used to represent the cylinder surface, is simulated an inertial effect promoted by body roughness.

The key idea of the roughness model capturing changes in the vortex shedding frequency (Strouhal number) is sketched in Figure 4a, where co_i represents a pivotal point and $eps_i(t)$ defines the location of a vortex blob, after its vorticity to be changed by surface roughness effect. The numerical effect of the roughness model is to change the core size, σ_0 , of each nascent vortex blob, using the following equation [21]:

$$\sigma_{0ck}(t) = 1.41421 \sqrt{\frac{\Delta t}{Re} \left(1 + \frac{v_{t_i}(t)}{v} \right)} \tag{11}$$

being Δt the temporal step estimated from velocity scale of the flow and Re the Reynolds number of the flow, as defined in Equation (1).

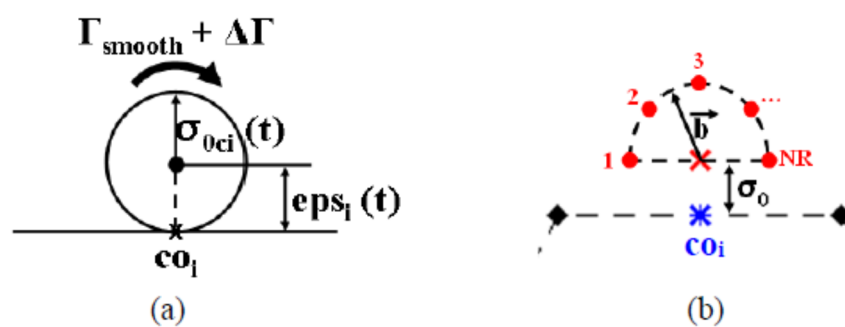


Figure 4. (a,b) Shedding of a vortex blob during one time stepping (co_i is the pivotal point and $eps_i(t)$ defines the “rough shedding point” location of the vortex blob).

In Equation (11), the local eddy viscosity coefficient computation newly depends on the solution of Equation (10). Therefore, the average velocity differences, required to calculate the second-order velocity structure function of the filtered field and to simulate surface roughness effect, are evaluated between the center of a semicircle with radius of $b = 2\varepsilon - \sigma_0$ and rough points, both placed near to each pivotal point, as follow [11]:

$$\bar{F}_{2_i}(t) = \frac{1}{NR} \sum_{w=1}^{NR} \|\bar{u}_{t_i}(x_i, t) - \bar{u}_{t_w}(x_i + \mathbf{b}, t)\|_w^2 (1 + \varepsilon) \tag{12}$$

where u_t is the instantaneous velocity filtered field, NR defines twenty-one rough points adjacent to each flat panel (Figure 4b), and $(1 + \varepsilon)$ characterizes the kinetic energy gain associated with the average roughness effect, $\varepsilon = \varepsilon^*/d^*$ (for more details, please see Bimbato et al. [11]).

2.5. Aerodynamic Loads

As previously commented in Section 2.3, the only governing equation in the discrete vortex method is the vorticity transport equation of the filtered field. It should be remarked that the pressure is missing in the formulation, because the pressure term is eliminated when is applied the curl in the

Navier–Stokes equations. The pressure filtered field is then recuperated by taking the divergence operator to the Navier–Stokes equations. The procedure starts with the stagnation pressure definition, such as:

$$\bar{Y}^* = \frac{\bar{p}^*}{\rho} + \frac{\bar{u}^{*2}}{2}, \quad \bar{u}^* = |\bar{\mathbf{u}}^*| \quad (13)$$

where \bar{p}^* defines the static pressure, ρ is the fluid density and $\bar{\mathbf{u}}^*$ represents the velocity.

Thus, a Poisson equation is derived, and the static pressure is obtained using an integral formulation, such as [39,40]:

$$H\bar{Y}_p - \int_{S_1+S_2} \bar{Y}\nabla\Xi_p \cdot \mathbf{e}_n dS = \iint_{\Omega} \nabla\Xi_p \cdot (\bar{\mathbf{u}} \times \bar{\boldsymbol{\omega}}) d\Omega - \frac{1}{Re} \int_{S_1} (\nabla\Xi_p \times \bar{\boldsymbol{\omega}}) \cdot \mathbf{e}_n dS \quad (14)$$

where p is the any point to compute pressure, $H = 1$ for points of the fluid domain, $H = 0.5$ for pivotal points, Ξ represents the fundamental solution of Laplace equation, and \mathbf{e}_n defines the unit vector normal to each solid boundary.

Finally, the drag and lift coefficients are calculated as, respectively [21]:

$$C_D = \sum_{p=1}^{NP} 2(\bar{p}_p - p_\infty)\Delta S_p \sin\beta_p = \sum_{p=1}^{NP} C_{p_p}\Delta S_p \sin\beta_p \quad (15)$$

$$C_L = - \sum_{p=1}^{NP} 2(\bar{p}_p - p_\infty)\Delta S_p \cos\beta_p = - \sum_{p=1}^{NP} C_{p_p}\Delta S_p \cos\beta_p \quad (16)$$

where NP represents the total number of flat panels, p_∞ represents the reference pressure at S_3 (Figure 1), ΔS_p defines a flat panel length, and β_p defines a flat panel angle.

2.6. Computational Sequence for Solution of the Navier–Stokes Equations

The numerical method described above is implemented to run sequentially according to the followings steps: (i) simultaneous generation of source panels and nascent vortex blobs (including the roughness model); (ii) calculation of the velocity vector at the point occupied by each vortex blob; (iii) calculation of surface pressure distribution and hence drag and lift on the cylinder; (iv) advection of the vortex blobs; (v) diffusion of the vortex blobs (including the LES modeling); (vi) reflection of the vortex blobs that migrate into the cylinder or ground plane; (vii) calculation of the velocity induced by vortex cloud at pivotal points; and (viii) advance by time Δt .

3. Results and Discussion

3.1. Simulation Setup

The chosen upper-subcritical Reynolds number for all computations was $Re = 1.0 \times 10^5$, which allows comparisons with experimental results presented by Nishino [25], when possible. Test cases were previously performed for the smooth circular cylinder aiming to find suitable values for the following parameters [21,22]: dimensionless time, $t = 75$; dimensionless time step, $\Delta t = 0.05$; number of nascent vortex blobs during each time step, $M = 300$; and initial displacement of each nascent vortex blob adjacent to the flat panel, $eps_i' = \sigma_{0i} = 0.001$, as illustrated in Figure 2.

The dimensionless time step was estimated according to $\Delta t = 2\pi K/N$, being $0 < K < 1$ and $N = 300$ [21,22] and it depends on the accuracy of the explicit Euler scheme; in this procedure N represents the number of flat panels adopted to discretize the cylinder surface [32]. All obtained values were computed in the interval $37.50 \leq t \leq 75.00$ to compute time-averaged results. The chosen dimensionless time step was found suitable to compute aerodynamic loads with accuracy reducing the final time of the simulations.

In Figure 1, the wall plane length was fixed as $L^*/d^* = 10$ and discretized using 950 flat panels. A horizontal distance of $L_l^*/d^* = 3$ allows to identify the cylinder front stagnation point, where the reference starts from the origin of inertial frame of reference placed at $(x^*/d^*; y^*/d^*) = (0.0; 0.0)$. That horizontal distance was previously investigated, being the length of $L_l^*/d^* = 3$ found suitable to capture the wall confinement (blockage) effect [21,22]. The blockage effect was captured when the gap-to-diameter ratio, h^*/d^* , was reduced from 0.80 to 0.05 (Tables 1 and 2). The relative roughness size of $\varepsilon^*/d^* = 0.001$ was chosen for the test cases, when the roughness model was activated. All the numerical results with no roughness model were identified by $\varepsilon^*/d^* = 0.000$ in Section 3.2.

Table 1. Experimental and numerical data of aerodynamic force coefficients for the circular cylinder in the vicinity of a moving wall ($Re = 1.0 \times 10^5$).

Gap-to-Diameter Ratio	Nishino [25] with No End Plates		Nishino [25] Using End Plates ($y_e^*/d^* = 0.00$)		Nishino [25] Using End Plates ($y_e^*/d^* = 0.40$)		Present Simulation ($\varepsilon^*/d^* = 0.000$)		Present Simulation ($\varepsilon^*/d^* = 0.001$)	
	C_D	C_L	C_D	C_L	C_D	C_L	C_D	C_L	C_D	C_L
h^*/d^*										
0.8	0.899	0.014	1.293	-0.02	1.385	0.024	1.38	0.092	1.284	0.04
0.6	0.92	0.039	1.302	0.001	1.373	0.038	1.408	0.105	1.437	0.103
0.5	0.924	0.045	1.282	0.034	1.323	0.09	1.474	0.104	1.459	0.104
0.45	0.926	0.06	1.242	0.054	1.311	0.102	1.443	0.108	1.392	0.105
0.4	0.922	0.074	1.145	0.084	-	-	1.433	0.058	1.454	-0.003
0.35	0.931	0.092	0.929	0.078	-	-	1.44	0.029	1.393	-0.002
0.3	0.93	0.117	0.941	0.111	-	-	1.426	-0.031	1.473	-0.026
0.25	0.933	0.144	0.951	0.154	-	-	1.455	-0.016	1.339	-0.041
0.2	0.939	0.177	0.954	0.188	-	-	1.435	0.004	1.278	-0.015
0.15	0.952	0.231	0.957	0.247	-	-	1.281	0.056	1.151	0.068
0.1	0.958	0.308	0.953	0.306	-	-	1.081	0.411	0.897	0.301
0.05	0.965	0.429	0.941	0.477	-	-	0.877	0.531	0.559	0.313

Table 2. Summary of data for the Strouhal number and position of separation for the circular cylinder in the vicinity of a moving wall ($Re = 1.0 \times 10^5$).

Gap-to-Diameter Ratio	Present Simulation ($\varepsilon^*/d^* = 0.000$)	Present Simulation ($\varepsilon^*/d^* = 0.001$)	Present Simulation ($\varepsilon^*/d^* = 0.000$)		Present Simulation ($\varepsilon^*/d^* = 0.001$)		Nishino [25] with No End Plates	
	St	St	θ^+_{sep}	θ^-_{sep}	θ^+_{sep}	θ^-_{sep}	θ^+_{sep}	θ^-_{sep}
h^*/d^*								
0.8	0.213	0.202	83°	88°	85°	90°	78°	82°
0.6	0.204	0.212	81°	88°	82°	95°	-	-
0.5	0.204	0.216	79°	91°	85°	96°	-	-
0.45	0.205	0.208	80°	92°	84°	99°	-	-
0.4	0.199	0.212	79°	93°	85°	97°	72°	92°
0.35	0.199	0.201	79°	95°	86°	98°	-	-
0.3	0.198	0.199	78°	94°	82°	99°	-	-
0.25	0.195	0.189	76°	95°	83°	100°	-	-
0.2	0.174	0.166	75°	97°	83°	104°	64°	91°
0.15	0.143	0.129	72°	99°	79°	104°	-	-
0.1	0.113	0.087	69°	100°	82°	100°	-	-
0.05	0.107	0.0	70°	103°	76°	102°	-	-

3.2. Circular Cylinder in the Vicinity of a Moving Wall

This section presents simultaneous measurements of integrated aerodynamic loads and surface pressure distributions for the circular cylinder, which are essentials to support all bellow discussions. The main objective is to report that the roughness model associated with blockage effect captures the full interruption of vortex shedding from the slightly rough cylinder surface placed closer to a moving wall. Thus, the results of drag force reduction, positive lift force, Strouhal number behavior, and location of the separations points of the flow around the cylinder will successfully support the analyses in a very good physical sense.

Table 1 presents experimental and numerical results of the aerodynamic force coefficients for the cylinder at upper-subcritical Reynolds number flows of $Re = 1.0 \times 10^5$. The experimental results are for the smooth cylinder case at different gap-to-diameter ratios, h^*/d^* , being the uncertainties in the drag, C_D , and lift, C_L , coefficients of ± 0.016 and ± 0.011 , respectively, with 95% confidence [25]. The goal is to compare them to our numerical results, also presented in Table 1.

The experimental results presented in Table 1 and identified as “using end plates” were obtained for the ratios of $y_e^*/d^* = 0.00$ and 0.40 . In the experiments of Nishino [25], the length y_e^* was defined as the distance from the edge of the cylinder to the bottom border of the end plate. In the experimental study, the bottom border of the end plate was placed below the cylinder, being the edge of the cylinder its bottom side ($\theta_{sep}^+ = 270^\circ$ in Figure 1).

With reference to Table 1, the experiments of Nishino [25] revealed that the drag force increases with the use of end plates for $h^*/d^* \geq 0.45$, i.e., the flow becomes more two-dimensional. The use of end plates with $y_e^*/d^* = 0.40$ revealed the flow closest to a two-dimensional pattern. The use of a pair of end plates, especially at high Reynolds numbers flows, was justified by Nishino [25] since the effect of the end condition of the cylinder cannot usually be large enough in practical investigations. As comparison, the numerical results of drag force for the smooth cylinder ($\varepsilon^*/d^* = 0.000$) present a very good agreement with the end plates configuration at $y_e^*/d^* = 0.40$, being the difference of the drag coefficient between them around 10%. When the small-gap regime is identified for $h^*/d^* < 0.20$, the drag force significantly reduces, and this behavior occurs because of the surface roughness effect. Lei et al. [23] observed that the critical drag behavior cannot be accurately determined, since experimental and numerical investigations are carried out using discrete gap-to-diameter ratios, and the vortex shedding suppression manifests as ratio h^*/d^* is gradually reduced. In general, the numerical results show that the lift force for the rough cylinder is slightly lower as compared as the smooth cylinder; that behavior agrees with observations [2].

Table 2 summarizes results of the Strouhal number, St , and separation point prediction, θ_{sep}^+ and θ_{sep}^- (Figure 1), for the same study cases shown in Table 1. There are no experimental data available of Strouhal number for the flow around smooth and rough cylinders near a moving wall. The experimental results for position of separation of the flow past the cylinder with no end plates [25] were included for comparison purposes. Nishino [25] did not report experimental results of the separation points prediction for the configuration of the cylinder using end plates at $y_e^*/d^* = 0.40$.

As illustration, the temporal history of the drag and lift coefficients of the smooth cylinder and other rough, both at $h^*/d^* = 0.50$ and 0.05 , is shown in Figure 5.

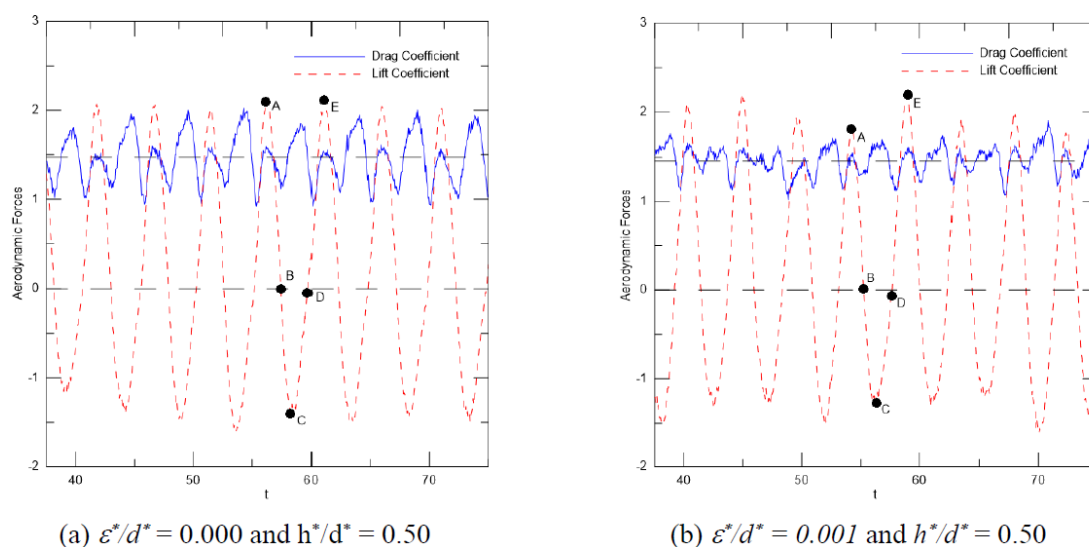


Figure 5. Cont.

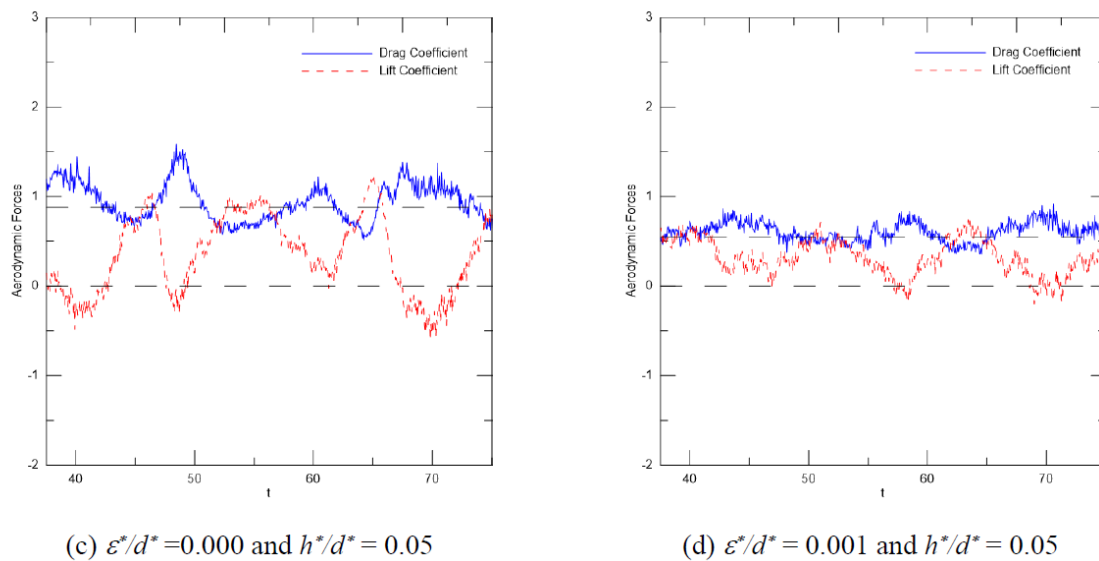


Figure 5. Temporal history of the drag and lift coefficients for the circular cylinder in the vicinity of a moving wall ($Re = 1.0 \times 10^5$).

Figure 6a,b present instantaneous pressure coefficient, C_p , distributions related to instants represented by points A–E, marked in Figure 5a,b, for the cylinder at $h^*/d^* = 0.50$. In Figure 6a,b, the separation angle on upper (open) side of the cylinder is identified as $\theta \equiv \theta^+_{sep}$.

In Figure 5a, the instant represented by point A characterizes a maximum value of the lift coefficient, where a clockwise vortical structure detaches from the smooth cylinder upper surface and moves toward the near wake (Figure 7a). That vortical structure grows and starts to attract the shear layer of opposite signal (Figure 7b). As consequence, a low pressure region is created at the cylinder upper surface (Figure 6a).

The instant represented by point C in Figure 5a indicates a minimum value of the lift coefficient, where a counter-clockwise vortical structure detaches from the smooth cylinder lower surface and moves toward the near wake. That vortical structure can be visualized in Figure 7c and it creates a low pressure region at the cylinder lower surface (Figure 6a). The same counter-clockwise vortical structure grows and starts to attract the shear layer of opposite signal (Figure 7d), the latter is feeding the clockwise vortical structure causing its detachment. It is important to observe that a new upper vortical structure will be born on the upper surface and will start to grow attracting the lower shear layer; the latter also will feed the lower vortical structure causing its detachment. The complete incorporation to the near wake of the lower and upper vortical structures is revealed at instants identified by points B and D in Figure 7b,d, respectively. In Figure 6a, the instant defined by point E represents the same event previously described for the point A.

The mechanism above reported is cyclic repeating alternatively on the upper and lower sides of the smooth cylinder surface. Thus, an unsteady flow with the presence of von Kármán-type vortices takes place downstream of the cylinder (Figure 8a). That phenomenon agrees to the classical vortex shedding mechanism of the smooth cylinder with no ground effect [41]. In Figure 8a, the viscous wake downstream takes the form of “mushroom-type” vortical structures, being that the blockage effect will destroy them far from the cylinder. For the large-gap regime, antisymmetrical perturbations are captured from the near wake region and they are felt near the cylinder surface. These perturbations intrinsically relate to the Von Kármán large-scale vortices formation mode.

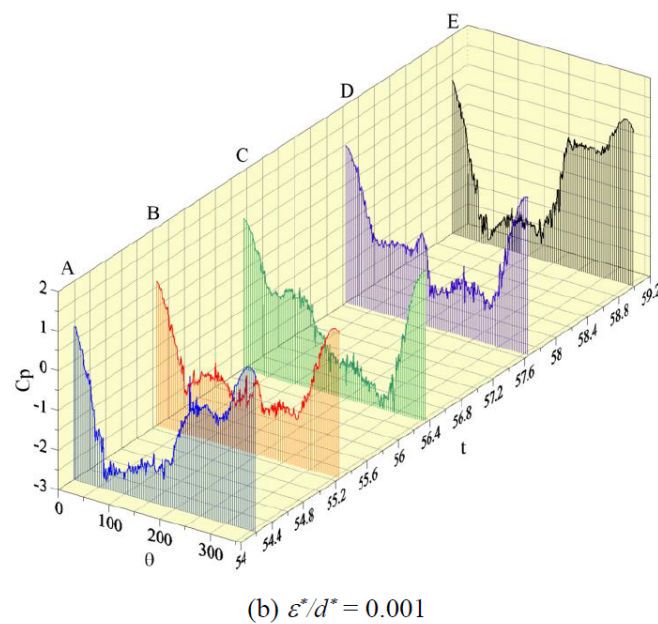
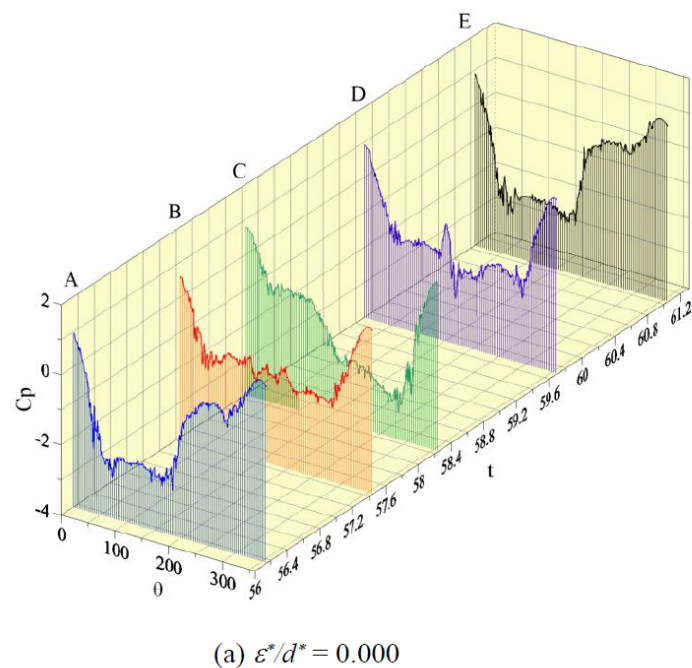


Figure 6. Instantaneous pressure distributions for the circular cylinder in the vicinity of a moving wall at $h^*/d^* = 0.50$ ($Re = 1.0 \times 10^5$).

Gerrard [41] stated that a vortical structure shedding from bluff body surface continues to grow (see, e.g., the upper vortical structure in Figure 7b), being fed by circulation originated of the connected shear layer and that, when it is strong enough, draws the opposing shear layer across the near wake. In this mechanism, the approximation of the shear layers of opposite signals is able to cut off further supply of circulation to the growing vortical structure, the latter, then, sheds and moves downstream the cylinder.

In this work, the mechanism of vortical structures formation at the rear part of the cylinder with no wall confinement [41] has also been identified for the smooth cylinder at $h^*/d^* = 0.50$ (Figure 7a–d).

Therefore, it can be concluded that the Venturi effect really redraws the lower vortical structure shed downstream. Figure 7c gives us an idea of the Venturi effect acting on a nascent vortical structure and deforming it.

The Venturi effect also contributes creating two different highest peaks for the drag coefficient curve, which is synchronized with the lift coefficient curve (Figure 5a). The explication for this interesting aerodynamic force behavior is that while the upper vortical structure finds total freedom to grow at the rear part of the cylinder until to be incorporated by the viscous wake (Figure 7b), leading to a bigger value in the drag coefficient (see approximately the drag coefficient value by projecting point C in Figure 5a), the developing of the lower vortical structure is affected by the Venturi effect (Figure 7c). This second event reflects the smaller peak in the drag curve (see approximately the drag coefficient value by projecting point D in Figure 5a).

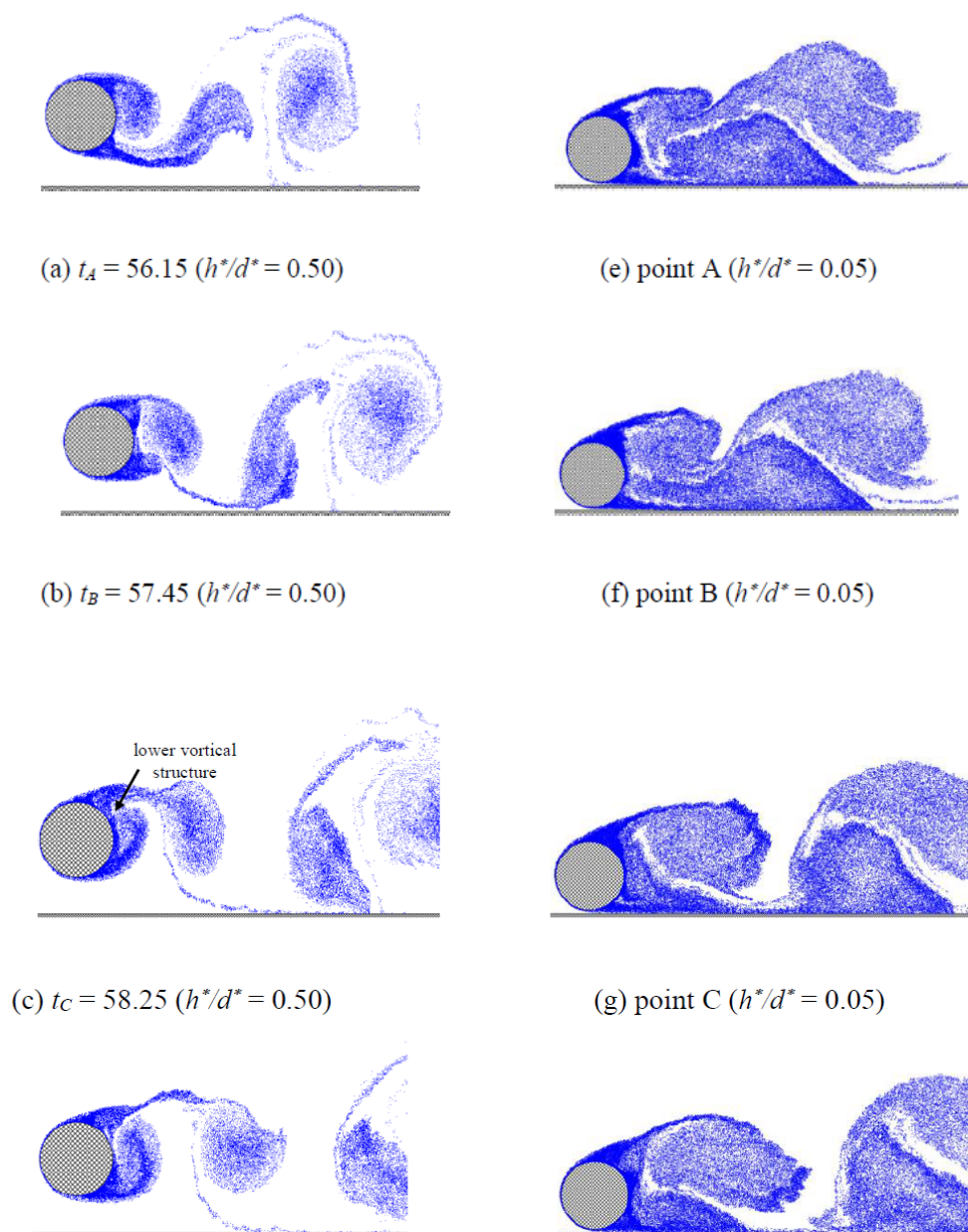


Figure 7. Near wake patterns for the circular cylinder in the vicinity of a moving wall ($\epsilon^*/d^* = 0.000$; $Re = 1.0 \times 10^5$).

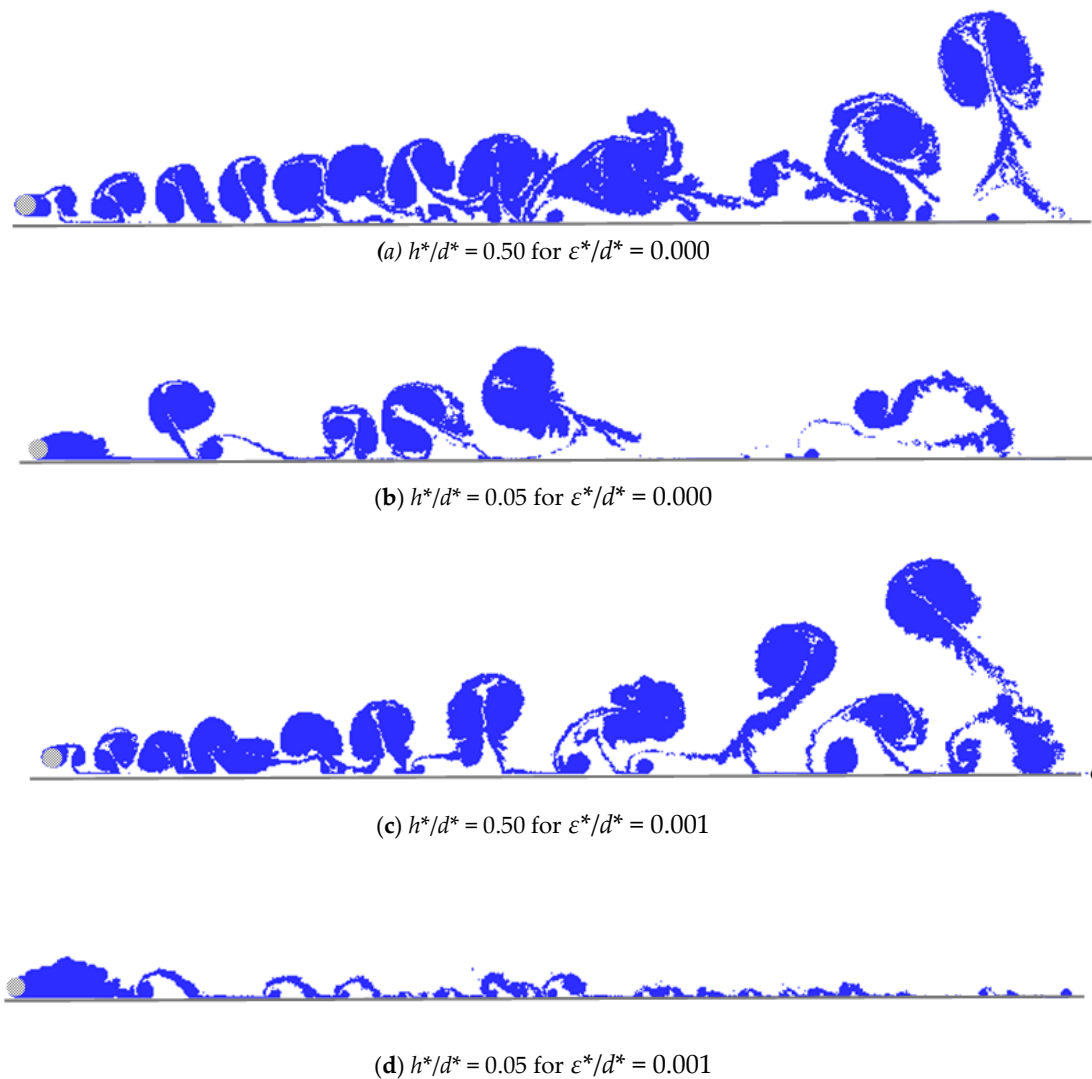


Figure 8. Final positions of clusters of vortex blobs for the circular cylinder in the vicinity of a moving wall at $t = 75$ ($Re = 1.0 \times 10^5$).

The study case for the smooth cylinder at $h^*/d^* = 0.50$ forecasts the occurrence of a (mean) stagnation point near the frontal part of the cylinder, where, at that position, the pressure coefficient is around 1.0 at $\theta \approx 0.6^\circ$ (Figure 6a). It is important to observe that the front stagnation point of the cylinder with no wall confinement is located at $\theta_{stag} = 0.6^\circ$ because the discretization of the cylinder surface using the panel method [32] initiates at $\theta = 0^\circ$, with the first pivotal point located at $\theta = 0.6^\circ$. The upper (open) separation angular position is identified at about $\theta_{sep}^+ \approx 79^\circ$ (Table 2). The experimental result for the smooth cylinder with no wall confinement at $Re = 1.0 \times 10^5$ is predicted around $\theta \approx 82^\circ$ [31]. The separation angle at bottom (gap) side is about $\theta_{sep}^- \approx 91^\circ$ (Table 2). This result is consistent with the expected physics for the problem because the wall confinement (blockage) effect really changes downstream the separation angle at cylinder bottom side. The experimental result of Nishino [25] for the cylinder with no end plates at $h^*/d^* = 0.40$ is predicted to occur about $\theta_{sep}^- \approx 92^\circ$ (Table 2). It is important to observe that a lower rear pressure (Figure 6a), identified for the cylinder in ground effect, reflects a higher value for the drag coefficient ($C_D \approx 1.474$ in Table 1) as compared to the experimental value reported by Blevins [31], that is $C_D \approx 1.2$, with 10% uncertainty. As additional information, a numerical result available in the literature [10] for smooth cylinder with no wall confinement is about $C_D \approx 1.198$.

The numerical result of the mean lift coefficient for the smooth cylinder at $h^*/d^* = 0.50$ is predicted around $C_L \approx 0.104$ (Table 1). The appearance of lift force pointing away from the moving wall is because of the viscosity effect, which definitively contributes to move the cylinder front stagnation point downstream and, as consequence, it is created an additional positive circulation with increasing of the lift force. This change on the front stagnation point is captured through the temporal history of points A–E in Figure 6a, in which a slight change can be identified (i.e., C_p is not more equal to 1.0 at $\theta = 0.6^\circ$). For the smooth cylinder with no wall confinement, the lift force oscillates around mean value of zero [10].

The numerical result of the Strouhal number for the cylinder at $h^*/d^* = 0.50$ seems insensitive to blockage effect, being predicted around $St \approx 0.204$ (Table 2). This conclusion is supported by the experimental value available in the literature for the smooth cylinder with no wall confinement at upper-subcritical flow regime of $Re = 1.0 \times 10^5$, that is around $St \approx 0.19$ [31], and also with 10% uncertainty. In accordance, the vortices formation mechanism [41] is not delayed, which justifies the Strouhal number value does not change. The latter conclusion is substantiated by defining the period $t_E - t_A$ corresponding to the detachment of a pair of vortical structures from cylinder surface and connected to each other by a vortex sheet, which rotate in opposite directions until they be completely incorporated into the viscous wake. The period computed is of $t_E - t_A = 61.15 - 56.15 = 5.0$ for the smooth cylinder at $h^*/d^* = 0.50$ (Figure 6a) and of $t_E - t_A = 4.7$ for the smooth cylinder with no wall confinement [10], being the difference between them around 6.0%.

The saturation state of a typical numerical simulation at dimensionless time of $t = 75$ can be demonstrated through of the difference around 2% between the Strouhal number, obtained from the inverse of the period $t_E - t_A \approx 0.20$ (Figure 6a), and other one of $St \approx 0.204$, which was computed from a Fast Fourier Transformation of the lift curve between $37.5 \leq t \leq 75$ (Figure 5a).

On the other hand, the temporal history of the drag and lift coefficients for the smooth cylinder at $h^*/d^* = 0.05$ can be seen in Figure 5c. The drag reduction is about 40.5% as compared as the smooth cylinder at $h^*/d^* = 0.50$ (Table 1). Figure 7e–h sketch the near wake pattern for the smooth cylinder at $h^*/d^* = 0.05$, being the instants defined by respective points A–D in Figure 9a. The Strouhal number reduces to $St \approx 0.107$ (Table 2), which characterizes intermittency on the von Kármán large-scale vortex formation mode (Figure 8b).

It is of great importance for the present work that the moving wall control demonstrates the efficiency of the roughness model to reduce the drag force of the rough cylinder, when the passive control technique of vortex shedding is activated, for the chosen relative roughness size of $\varepsilon^*/d^* = 0.001$ (Figure 5b,d can be compared). The hybrid control technique is therefore able to reduce the drag force of the smooth cylinder at $h^*/d^* = 0.50$ around 62.1% as compared as the rough cylinder at $h^*/d^* = 0.05$ (from $C_D \approx 1.474$ to 0.559 in Table 1). It is interesting to comment that Alcântara Pereira et al. [10] also identified a strong reduction on the drag force when using the relative roughness size of $\varepsilon^*/d^* = 0.007$ at $h^*/d^* < 0.20$ (small-gap regime). In their numerical experiment, the drag force of the rougher cylinder at $h^*/d^* = 0.05$ reduced around 60.2% as compared as the smooth cylinder near a moving wall at $h^*/d^* = 0.50$. In both numerical studies, the higher drag reduction is because of the passive control technique promoting the full interruption on the von Kármán large-scale vortices formation mode.

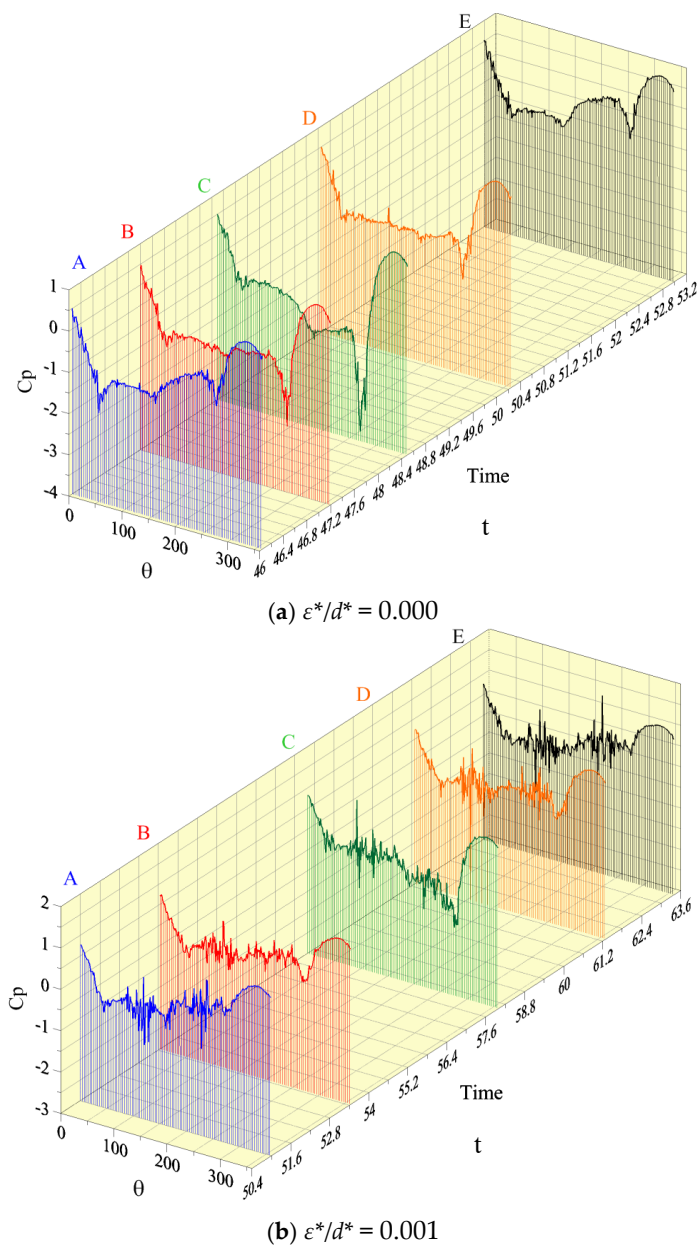


Figure 9. Instantaneous pressure distributions for the circular cylinder in the vicinity of a moving wall at $h^*/d^* = 0.05$; $Re = 1.0 \times 10^5$.

The rough cylinder at $h^*/d^* = 0.05$ configuration is strongly sensitive to interfere to the Venturi effect, which controls the smooth cylinder aerodynamics when submitted to ground effect. The surface roughness effect also participates to control the flow dynamics of the cylinder. The lift coefficient reduces of $C_L \approx 0.531$ (smooth case) for $C_L \approx 0.313$ (rough case), a reduction of 41.1% (Table 1).

Figure 5b shows that the surface roughness effect interferes on the orderly behavior of the big and small peaks previously identified in the drag curve for the smooth cylinder at $h^*/d^* = 0.50$ (Figure 5a). Now, in Figure 5b, there are no more single big and small peaks as the dimensionless time runs from $t = 40$ on, approximately. In Figure 5b, it is until difficult to identify the big and small peaks in the drag curve because of noise increasing originated from roughness effect. The period $t_E - t_A$ is of 5.0 in Figure 6b, and of $t_E - t_A = 4.7$ for the cylinder with no wall confinement [10]. Once again, the difference between them is around 6.0%, and the suppression of vortex shedding cannot be promoted when using $\varepsilon^*/d^* = 0.001$ at $h^*/d^* = 0.50$ (Figure 8c).

Figure 9b presents instants randomly chosen and represented by points A–E for instantaneous pressure distributions of the rough cylinder at $h^*/d^* = 0.05$. The simulation also predicts the appearing of a (mean) stagnation point near the cylinder frontal part, where, at that position, the pressure coefficient, C_p , is not more 1.0 at $\theta = 0.6^\circ$ (Figure 9b). In Figure 5d, it is more difficult to identify points A–E as compared as the Figure 5a.

The Strouhal number completely vanishes, $St = 0.0$, for the cylinder with roughness model at $h^*/d^* = 0.05$ (Table 2). Bimbato et al. [22] also identified a decrease of the Strouhal number for the smooth cylinder at $h^*/d^* = 0.05$, however, in their numerical experiment, the Strouhal number did not vanish ($St \approx 0.080$). In the present simulation, the correspondent computed value was of $St \approx 0.107$ (Table 2). An important conclusion is that for the smooth cylinder placed too close of the moving wall, i.e., at $h^*/d^* = 0.05$, the full interruption of von Kármán-type vortex shedding is not captured only using the active control technique by moving wall (Figure 7e–h).

The Strouhal number behavior was reported by Buresti and Lanciotti [12] for smooth and rough cylinders near a fixed ground at Reynolds numbers in the range from $Re = 8.5 \times 10^4$ to 3.0×10^5 . The boundary layer thickness on the ground was about $\delta^*/d^* = 0.1$ at cylinder location. For the flow around the smooth cylinder, within the subcritical and critical regimes ($Re < 1.9 \times 10^5$), the critical gap-to-diameter ratio, h^*/d^* , was identified at 0.40, and the Strouhal number was estimated around of 0.20 for all ratios h^*/d^* greater than 0.40. The same results were obtained within the subcritical and critical regimes (in this situation, $Re < 1.4 \times 10^5$ because of the surface roughness effect) also for the rough cylinder. Although there is a lack of experimental data of Strouhal number for the flow around the smooth and rough cylinders near a moving wall, our numerical results agree basically with an experimental result of $St \approx 0.20$ for the cylinder near a fixed ground at large-gap regime. For the small-gap regime at $h^*/d^* < 0.20$, the Strouhal number decreases, and the boundary layer separation is delayed because of the combined effects of surface roughness and wall confinement (Table 2).

Figure 10a–h can be accompanied in sequence to better understand both interferences of surface roughness and wall confinement, which combined, completely destroy the orderly von Kármán vortex street. Instead, the Venturi effect interferes redrawing the negative shear layer parallel to ground plane behind the rough cylinder at $h^*/d^* = 0.05$. Figures 8d and 10e–h sketch the near wake pattern of the rough cylinder at $h^*/d^* = 0.05$, being the instants defined by points A–D in Figure 9b.

The difference of drag reduction between the study cases at $h^*/d^* = 0.05$ is explained because the base pressure increases for the rough cylinder (Figure 11b). It can be identified a lesser increase in the base pressure of the smooth cylinder (Figure 11a), which explains the difference about 36.3% in the drag force between them (Table 1).

Further numerical investigation will be carried out elsewhere to fully understand the relationship of the instantaneous surface pressure behavior with the mutual interaction between the two layers of opposite signals, when the complete interruption of vortex shedding is anticipated, for the rough cylinder at $h^*/d^* = 0.05$. Figures 8d and 10e–h give us some hints. Some small vortical structures observed in Figure 8d has been formed because of the two shear layers of opposite signals injecting vorticity at the rear part of the cylinder. As captured in our animations, the advection of vorticity of signals positive and negative creates those small vortical structures.

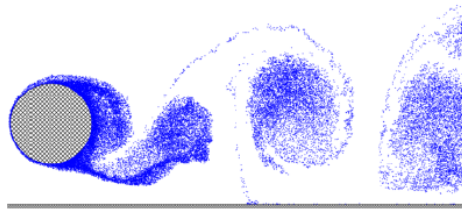
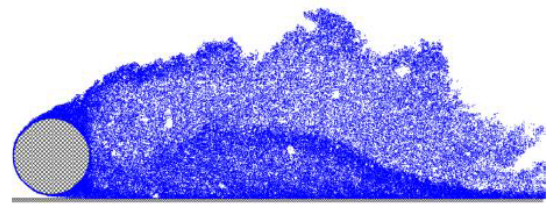
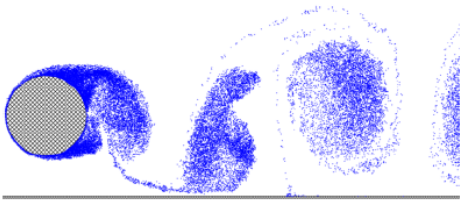
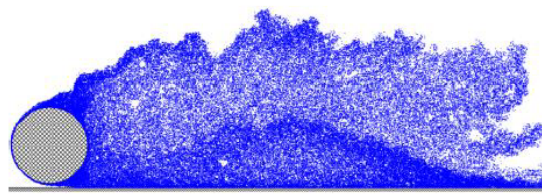
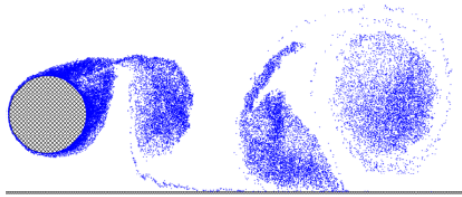
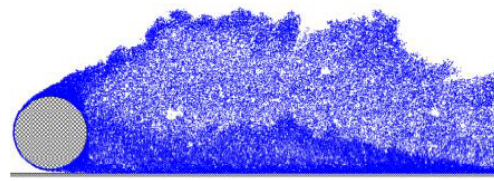
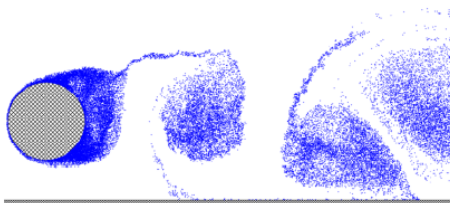
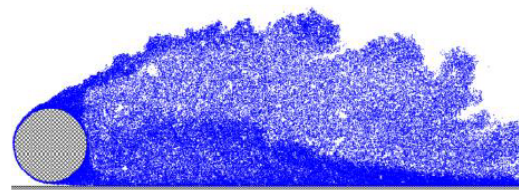
(a) $t_A = 54.20$ ($h^*/d^* = 0.50$)(e) point A ($h^*/d^* = 0.05$)(b) $t_B = 55.25$ ($h^*/d^* = 0.50$)(f) point B ($h^*/d^* = 0.05$)(c) $t_C = 56.35$ ($h^*/d^* = 0.50$)(g) point C ($h^*/d^* = 0.05$)(d) $t_D = 57.65$ ($h^*/d^* = 0.50$)(h) point D ($h^*/d^* = 0.05$)

Figure 10. Near wake patterns for the slightly rough circular cylinder in the vicinity of a moving wall ($\epsilon^*/d^* = 0.001$; $Re = 1.0 \times 10^5$).

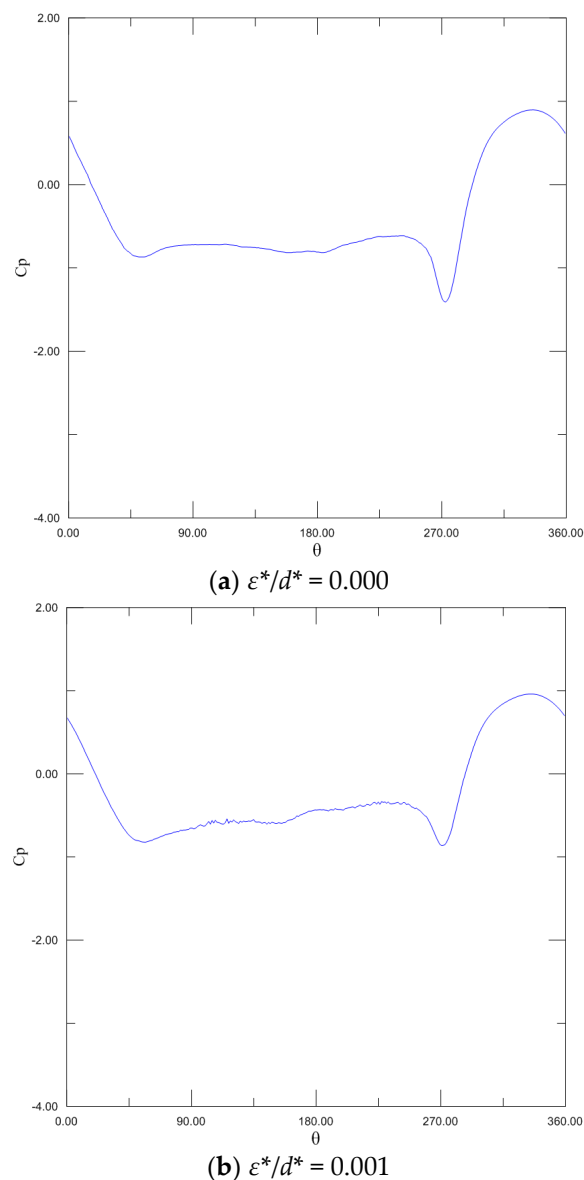


Figure 11. Time-averaged pressure distributions for the circular cylinder in the vicinity of a moving wall ($h^*/d^* = 0.05$; $Re = 1.0 \times 10^5$).

4. Conclusions

The present numerical study was addressed for the control and suppression of vortex shedding from a slightly rough bluff body in the vicinity of moving wall. A discrete vortex method implemented with a hybrid control technique of vortex shedding was employed. The association of active and passive control techniques of vortex shedding to study the two-dimensional flow past the rough circular cylinder placed too close to a moving wall (i.e., for the gap spacing of $h^*/d^* = 0.05$ in Figure 1) successfully captured the complete interruption of von Kármán-type vortex shedding (Figure 8d). The philosophy of our research line is to attain supercritical Reynolds number flow patterns starting from subcritical flows [11]. Achenbach [9] presented a classical $\overline{C}_D \times Re$ diagram (being \overline{C}_D the mean drag coefficient) for the circular cylinder, and divided it into four flow regimes, i.e., subcritical ($Re < 2.0 \times 10^5 - 5.0 \times 10^5$), critical ($Re \approx 2.0 \times 10^5 - 5.0 \times 10^5$), supercritical ($2.0 \times 10^5 - 5.0 \times 10^5 < Re \leq 3.5 \times 10^6$) and transcritical ($Re > 3.5 \times 10^6$), being the latter nowadays called post-critical. The numerical results reported in the present work have been substantiated by experimental data of the flow past

the smooth cylinder in the vicinity of a moving wall at upper-subcritical Reynolds number flow of $Re = 1.0 \times 10^5$ [25]. The key findings of the present study are summarized below.

- (a) The most important result obtained for the rough cylinder is the decrease in its drag force and, as consequence, the delay in the boundary layer separation as the ratio h^*/d^* reduces (Table 2). The drag reduction is substantiated by an increase in the base pressure of the cylinder as compared as the smooth cylinder configuration (Figure 11a,b).
- (b) The appearance of lift force pointing away from the moving wall is identified as the ratio h^*/d^* reduces (Table 1). This result is because of viscosity effect, which moves the cylinder front stagnation point downstream and creates an additional positive circulation contributing to increase the lift force (e.g., Figure 11a,b).
- (c) The surface roughness effect on the cylinder at $h^*/d^* = 0.05$ is the key factor to anticipate the complete interruption of vortex shedding suppression, and, thus, the Strouhal number completely vanishes ($St = 0.0$ in Table 2); also two nearly parallel shear layers of opposite signals are created at the rear part of the cylinder (Figure 10e–h), being that the Venturi effect definitively contributes to redraw the negative shear layer parallel to the wall plane.
- (d) The critical Strouhal number behavior for the rough cylinder at $h^*/d^* = 0.05$ is directly connected to a global change in its viscous wake structure (Figure 8d). In past work by Bimbatto et al. [22], the full interruption of the formation of Von Kármán large-scale vortices was not captured for the flow past the smooth cylinder in the vicinity of a moving wall at $h^*/d^* = 0.05$ (Figure 8b,d can be used to comparison between test cases). Alcântara Pereira et al. [10] reported that the complete interruption of vortex shedding for the cylinder can be anticipated using a relative roughness size of $\varepsilon^*/d^* = 0.007$ at $h^*/d^* = 0.10$. Therefore, the present work also completes the past study of Alcântara Pereira et al. [10], now including discussions for the slightly rough cylinder with relative roughness size of $\varepsilon^*/d^* = 0.001$.
- (e) The saturation state of a typical numerical simulation at dimensionless time of $t = 75$ is demonstrated through of the difference about 2% between Strouhal number values, one of them obtained from the inverse of the period $t_E - t_A$ (Figure 6a,b and Figure 9a,b), and other one computed from a Fast Fourier Transformation of the lift curve between $37.5 \leq t \leq 75$ (Figure 5a,d).
- (f) The work also highlights vortex shedding partial suppression with representative reduction of both the Strouhal number (Table 1) and fluctuating drag and lift forces (Figure 5a,b).
- (g) The present results suggest the applicability of the discrete vortex method with two-dimensional roughness model to study flows involving vortex shedding, and its control and suppression, from a bluff body in many practical problems, such as vibration of pipelines, transmission lines, suspension bridges, buildings, (semi-) submerged oil platform columns, heat exchangers tubes, periscopes and so on.
- (h) The physical interpretations that have been presented in the present approach also contribute to report the sensitivity of the roughness model. It can be pointed that it is successfully captured and numerical simulations with acceptable accuracy for practical engineering applications can be performed.

Author Contributions: Conceptualization, M.A.d.O., C.L.d.A., and L.A.A.P.; data curation, M.A.d.O., P.G.d.M., and C.L.d.A.; formal analysis, C.L.d.A., A.M.B., and L.A.A.P.; funding acquisition, L.A.A.P.; investigation, M.A.d.O., P.G.d.M., C.L.d.A., and A.M.B.; methodology, C.L.d.A., A.M.B., and L.A.P.P.; project administration, A.M.B. and L.A.A.P.; resources, C.L.d.A. and L.A.A.P.; software using FORTRAN, C.L.d.A. and A.M.B.; validation, M.A.d.O., P.G.d.M., and C.L.d.A.; visualization, M.A.d.O., P.G.d.M., and C.L.d.A.; supervision, L.A.A.P.; writing—original draft, L.A.A.P.; and writing—review and editing, A.M.B. and L.A.A.P. All authors have read and agreed to the published version of the manuscript.

Funding: This research was supported by the FAPEMIG through the research project APQ-02175-14.

Conflicts of Interest: The authors declare no conflict of interest.

References

1. Bearman, P.W. Vortex shedding from oscillating bluff body. *Ann. Rev. Fluid Mech.* **1984**, *16*, 195–222. [[CrossRef](#)]
2. Gao, Y.; Fu, S.; Wang, J.; Song, L.; Chen, Y. Experimental study of the effects of surface roughness on the vortex-induced vibration of a flexible cylinder. *Ocean Eng.* **2015**, *103*, 40–54. [[CrossRef](#)]
3. Hirata, M.H.; Alcântara Pereira, L.A.; Recicar, J.N.; Moura, W.H. High Reynolds number oscillations of a circular cylinder. *J. Braz. Soc. Mech. Sci. Eng.* **2008**, *30*, 304–312. [[CrossRef](#)]
4. Hong, K.S.; Shah, U.M. Vortex-induced vibrations and control to marine risers: A review. *Ocean Eng.* **2018**, *152*, 300–315. [[CrossRef](#)]
5. Ma, W.; Liu, Q.; Macdonald, J.H.G.; Yan, X.; Zeng, Y. The effect of surface roughness on aerodynamic forces and vibrations for a circular cylinder in the critical Reynolds number range. *J. Wind Eng. Ind. Aerodyn.* **2019**, *187*, 61–72. [[CrossRef](#)]
6. Sun, H.; Ma, C.; Kim, E.O.; Nowakowski, G.; Bernitsas, M.M. Flow-induced vibration of tandem circular cylinders with selective roughness: Effect of spacing, damping and stiffness. *Eur. J. Mech. B/Fluids* **2019**, *74*, 219–241. [[CrossRef](#)]
7. Faure, T.M.; Dumas, L.; Montagnier, O. Numerical study of two-airfoil arrangements by a discrete vortex method. *Theor. Comput. Fluid Dyn.* **2020**, *34*, 79–103. [[CrossRef](#)]
8. Los Reis, J.H.; Alcântara Pereira, L.A. Particle-particle interactions in parallel computations. In Proceedings of the 16th Brazilian Congress of Thermal Sciences and Engineering, Vitoria, ES, Brazil, 7–10 November 2016.
9. Achenbach, E. Influence of surface roughness on the cross-flow around a circular cylinder. *J. Fluid Mech.* **1971**, *46*, 321–335. [[CrossRef](#)]
10. Alcântara Pereira, L.A.; Oliveira, M.A.; Moraes, P.G.; Bimbato, A.M. Numerical experiments of the flow around a bluff body with and without roughness model near a moving wall. *J. Braz. Soc. Mech. Sci. Eng.* **2020**, *42*, 129. [[CrossRef](#)]
11. Bimbato, A.M.; Alcântara Pereira, L.A.; Hirata, M.H. Development of a new Lagrangian vortex method for evaluating effects of surface roughness. *Eur. J. Mech. B/Fluids* **2019**, *74*, 291–301. [[CrossRef](#)]
12. Buresti, G.; Lanciotti, A. Vortex shedding from smooth and roughened cylinders in cross-flow near a plane surface. *Aeronaut. Q.* **1979**, *30*, 305–321. [[CrossRef](#)]
13. Buresti, G. The effect of surface roughness on the flow regime around circular cylinders. *J. Wind Eng. Ind. Aerodyn.* **1981**, *8*, 105–114. [[CrossRef](#)]
14. Fage, A.; Warsap, J.H. *The Effects of Turbulence and Surface Roughness on the Drag of a Circular Cylinder*; H.M. Stationary Office: London, UK, 1929.
15. Gupta, A.; Saha, A.K. Suppression of vortex shedding in flow around a square cylinder using control cylinder. *Eur. J. Mech. B/Fluids* **2019**, *76*, 276–291. [[CrossRef](#)]
16. Guven, O.; Farrell, C.; Patel, V.C. Surface roughness effects on the mean flow past circular cylinders. *J. Fluid Mech.* **1980**, *98*, 673–701. [[CrossRef](#)]
17. Kareem, A.; Cheng, C.M. Pressure and force fluctuations on isolated roughened circular cylinders of finite height in boundary layer flows. *J. Fluids Struct.* **1999**, *13*, 907–934. [[CrossRef](#)]
18. van Hinsberg, N.P. The Reynolds number dependency of the steady and unsteady loading on a slightly rough circular cylinder: From subcritical up to high transcritical flow state. *J. Fluids Struct.* **2015**, *55*, 526–539. [[CrossRef](#)]
19. Yamagishi, Y.; Oki, M. Effect of groove shape on flow characteristics around a circular cylinder with grooves. *J. Vis.* **2004**, *7*, 209–216. [[CrossRef](#)]
20. Rashidi, S.; Hayatdavoodi, M.; Esfahani, J.A. Vortex shedding suppression and wake control. *Ocean Eng.* **2016**, *126*, 57–80. [[CrossRef](#)]
21. Bimbato, A.M.; Alcântara Pereira, L.A.; Hirata, M.H. Study of the vortex shedding flow around a body near a moving ground. *J. Wind Eng. Ind. Aerodyn.* **2011**, *99*, 7–17. [[CrossRef](#)]
22. Bimbato, A.M.; Alcântara Pereira, L.A.; Hirata, M.H. Suppression of vortex shedding on a bluff body. *J. Wind Eng. Ind. Aerodyn.* **2013**, *121*, 16–28. [[CrossRef](#)]
23. Lei, C.; Cheng, L.; Kavanagh, K. Re-examination of the effect of a plane boundary on force and vortex shedding of a circular cylinder. *J. Wind Eng. Ind. Aerodyn.* **1999**, *80*, 263–286. [[CrossRef](#)]

24. Li, Z.; Lan, C.; Jia, L.; Ma, Y. Ground effects on separated laminar flows past an inclined flat plate. *Theor. Comput. Fluid Dyn.* **2017**, *31*, 127–136. [[CrossRef](#)]
25. Nishino, T. Dynamics and Stability of Flow Past a Circular Cylinder in Ground Effect. Ph.D. Thesis, Faculty of Engineering Science and Mathematics, University of Southampton, Southampton, UK, 2007.
26. Roshko, A.; Steinolfson, A.; Chattoorgoon, V. Flow forces on a cylinder near a wall or near another cylinder. In Proceedings of the 2nd US Nation Conference on Wind Engineering Research, Fort Collins, CO, USA, 22–25 June 1975.
27. Zdravkovich, M.M. Forces on a circular cylinder near a plane wall. *Appl. Ocean Res.* **1985**, *7*, 197–201. [[CrossRef](#)]
28. Zdravkovich, M.M. *Flow around Circular Cylinders. Volume 2: Applications*; Oxford University Press: Oxford, UK, 2003.
29. Cui, E.; Zhang, X. Ground effect aerodynamics (Chapter 18). In *Encyclopedia of Aerospace Engineering*; John Wiley & Sons, Ltd.: Hoboken, NJ, USA, 2010.
30. Zhang, X.; Toet, W.; Zerihan, J. Ground effect aerodynamics of race cars. *ASME Appl. Mech. Rev.* **2006**, *59*, 33–49. [[CrossRef](#)]
31. Blevins, R.D. *Applied Fluid Dynamics Handbook*; Van Nostrand Reinhold Co.: Hoboken, NJ, USA, 1984.
32. Katz, J.; Plotkin, A. *Low Speed Aerodynamics: From Wing Theory to Panel Methods*; McGraw Hill Inc.: New York, NY, USA, 1991.
33. Kundu, P.K. *Fluid Mechanics*; Academic Press: Cambridge, UK, 1990.
34. Leonard, A. Vortex methods for flow simulation. *J. Comp. Phys.* **1980**, *37*, 289–335. [[CrossRef](#)]
35. Chorin, A.J. Numerical study of slightly viscous flow. *J. Fluid Mech.* **1973**, *57*, 785–796. [[CrossRef](#)]
36. Alcântara Pereira, L.A.; Hirata, M.H.; Silveira Neto, A. Vortex method with turbulence sub-grid scale modeling. *J. Braz. Soc. Mech. Sci. Eng.* **2003**, *25*, 140–146.
37. Helmholtz, H. On integrals of the hydrodynamics equations which express vortex motion. *Philos. Mag.* **1867**, *33*, 485–512. [[CrossRef](#)]
38. Lesieur, M.; Métais, O. New trends in large eddy simulation of turbulence. *Annu. Rev. Fluid Mech.* **1996**, *28*, 45–82. [[CrossRef](#)]
39. Alcântara Pereira, L.A.; Hirata, M.H.; Manzanara Filho, N. Wake and aerodynamics loads in multiple bodies: Application to turbomachinery blade rows. *J. Wind Eng. Ind. Aerodyn.* **2004**, *92*, 477–491. [[CrossRef](#)]
40. Shintani, M.; Akamatsu, T. Investigation of two-dimensional discrete vortex method with viscous diffusion model. *CFD J.* **1994**, *3*, 237–254.
41. Gerrard, J.H. The mechanics of the formation region of vortices behind bluff bodies. *J. Fluid Mech.* **1966**, *25*, 401–413. [[CrossRef](#)]

